

Advances in the numerical treatment of grain-boundary migration: Coupling with mass transport and mechanics

Hashem M. Mourad^{1,2}, Krishna Garikipati²

*Department of Mechanical Engineering, University of Michigan
Ann Arbor, Michigan 48109, USA*

Abstract

This work is based upon a coupled, atomically-based continuum formulation that was previously applied to problems involving strong coupling between mechanics and mass transport; e.g. diffusional creep and electromigration [1, 2]. Here we discuss an enhancement of this formulation to account for migrating grain boundaries. The treatment is based on the level set method and can easily be generalized to model other problems with migrating interfaces; e.g. void evolution and free-surface morphology evolution. The level-set formulation developed is remarkably simple and obviates the need for spatial stabilization. It also makes use of velocity extension, field re-initialization and least-squares smoothing techniques. The latter allow the local curvature of a grain boundary to be computed directly from the level-set field without resorting to higher-order interpolation. A notable feature is that the coupling between mass transport, mechanics and grain-boundary migration is fully accounted for. The complexities associated with this coupling are highlighted and the operator-split algorithm used to solve the coupled equations is described.

Key words: Grain-boundary migration, level set method, self-diffusion.

1 Introduction

In a recent paper, Garikipati *et al.* [1] presented a coupled continuum field formulation for the interaction of self-diffusion, mechanics and electromigration in polycrystalline solids. Computational techniques were developed based upon the finite element method. Their approach drew upon earlier work by Larché

¹*Present address:* Department of Civil and Environmental Engineering, Duke University Durham, North Carolina 27708, USA.

²*Email addresses:* H. Mourad <hmourad@duke.edu>, K. Garikipati <krishna@umich.edu>

and Cahn [3, 4], Nix and Co-workers [5, 6], Génin [7], Bower and Freund [8], Xia *et al.* [9]—to name but a few. A review of these and other works appeared in [1]. Several initial- and boundary-value problems, involving diffusional creep (Nabarro-Herring and Coble creep), were solved. The formulation was extended to interdiffusion, with dopants in silicon as motivation, by Garikipati and Bassman [2]. In the current paper, we present a further extension of this formulation to self-diffusion in the presence of migrating grain boundaries.

Different strategies have been used to model grain-boundary motion in a computational setting. Sun and Suo [10, 11] developed a two-dimensional finite element formulation, based on the idea that the energy dissipated during the motion of the boundary must equal the reduction in the free energy of the system. This formulation was used to study several problems including grain growth in a thin film and the competition between surface grooving and grain-boundary migration. A similar variational formulation was developed by Cocks and Gill [12, 13] and used to model the evolution of a large network of grains in two dimensions. Another model was developed by Zhao *et al.* [14], based on the variational formulation of Reitich and Soner [15] and using the level set method of Osher and Sethian [16], which is also used in the current paper.

The goal of the current work is not merely to simulate grain-boundary motion, but to capture fully the interaction between this motion and other microscale phenomena that take place in pure polycrystalline materials, namely stress-mediated self-diffusion and electromigration. In Section 2, we summarize the formulation for coupled mass transport and mechanics. Then we examine the thermodynamics and kinetics of grain-boundary migration, and show how this phenomenon interacts with mass transport and mechanics in polycrystals. In Section 3, we formulate the grain-boundary migration problem using the level set method and we describe the computational methods used in the implementation of this formulation. Numerical examples are presented in Section 4. A summary is provided and conclusions are drawn in Section 5.

2 The coupled formulation

2.1 Thermodynamic basis

The thermodynamics is posed in a continuum setting, with motivation provided by atomic processes. A schematic of the lattice is shown in Fig. 1. It shows atoms, vacancies, and a free surface; the latter is a source and sink for vacancies. A grain boundary could serve as a source or sink also. Free surfaces and grain boundaries are treated as regions of finite width, δ_s and $2\delta_{gb}$ respectively.

2.1.1 Internal energy density

We consider crystalline materials in which the dangling bonds around a vacancy cause an inward relaxation of the surrounding lattice (see Fig. 1). The resulting

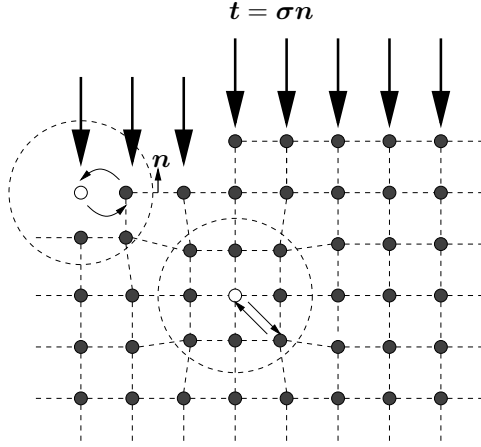


Figure 1: Schematic rendering of a lattice with atoms and vacancies.

vacancy relaxation strain can be expressed as

$$\boldsymbol{\varepsilon}^v = -\frac{1}{3}(1-f)\Omega(C_v - C_{v_0}^{eq})\mathbf{1}, \quad (1)$$

where Ω is the atomic volume, $f\Omega$ (with $0 < f < 1$) is the volume of a vacancy, C_v is the vacancy concentration, $C_{v_0}^{eq}$ is the vacancy concentration at thermodynamic equilibrium under vanishing external stress and $\mathbf{1}$ is the second-order isotropic tensor. The creep strain resulting from the accumulation or depletion of atoms at a free surface or grain boundary with unit normal, \mathbf{n} , can be expressed as

$$\boldsymbol{\varepsilon}^c = \frac{1}{3}\theta_c(\mathbf{n} \otimes \mathbf{n}). \quad (2)$$

A non-phenomenological evolution equation for θ_c was derived and discussed in detail by Garikipati *et al.* [1]. The thermal strain is given by

$$\boldsymbol{\varepsilon}^{th} = \alpha(T - T_0)\mathbf{1}, \quad (3)$$

where T is the temperature, T_0 is a reference temperature and α is the linear coefficient of thermal expansion. The elastic strain is obtained by subtracting these inelastic strain contributions from the total strain, $\boldsymbol{\varepsilon}$; i.e.

$$\boldsymbol{\varepsilon}^e = \boldsymbol{\varepsilon} - (\boldsymbol{\varepsilon}^v + \boldsymbol{\varepsilon}^c + \boldsymbol{\varepsilon}^{th}). \quad (4)$$

The stress is obtained from the elastic strain and the (generally anisotropic) fourth-order elasticity tensor, \mathbb{C} , as

$$\boldsymbol{\sigma} = \mathbb{C} : \boldsymbol{\varepsilon}^e. \quad (5)$$

Given a state with local stress, $\boldsymbol{\sigma}$, the incremental elastic strain energy density is then given as $\boldsymbol{\sigma} : \delta\boldsymbol{\varepsilon}^e = (\mathbb{C} : \boldsymbol{\varepsilon}^e) : \delta\boldsymbol{\varepsilon}^e$, where $\delta\boldsymbol{\varepsilon}^e$ is the increment in elastic strain.

With this background, the incremental internal energy density δe , corresponding to a state $\{\boldsymbol{\varepsilon}, T, C_v\}$, and increments $\delta\boldsymbol{\varepsilon}$ and δC_v is

$$\delta e = \delta \hat{e}_\eta(\eta) + e_v^f \delta C_v + (\mathbb{C} : \boldsymbol{\varepsilon}^e) : \delta \boldsymbol{\varepsilon}^e, \quad (6)$$

where η is the entropy density and e_v^f is the vacancy formation energy. The specific form of $\hat{e}_\eta(\eta)$, the entropic dependence of e , is not important to the development that follows.

2.1.2 External work density

The density of work done by external agents can be expressed as

$$\delta w_{ext} = \boldsymbol{\sigma} : \delta \boldsymbol{\varepsilon} - q\psi \delta C_v + \frac{3}{2}(\mathbf{n} \cdot \boldsymbol{\sigma} \mathbf{n}) f \Omega \delta C_v \chi. \quad (7)$$

Here, the first term of the right-hand side is the classical stress-power term. The second term accounts for the apparent work performed by the electrostatic potential, ψ , during electromigration; in this phenomenological treatment, q is the apparent charge ascribed to each vacancy. The last term accounts for the work done against the stress when vacancies are created at a free surface or grain boundary. The numerical factor appearing in this term arises from geometrical considerations. Additionally, the requirement that this term be active only at sources and sinks is enforced using the indicator function, χ , defined as

$$\chi(\mathbf{x}, t) = \begin{cases} 1 & \text{if } \mathbf{x} \text{ is in a surface- or grain-boundary region,} \\ 0 & \text{otherwise.} \end{cases} \quad (8)$$

2.1.3 Entropy density

The total entropy density is given by

$$\eta = \hat{\eta}_{vib}(T) - k \left[C_v \log \left(\frac{C_v}{C_s} \right) + C_a \log \left(\frac{C_a}{C_s} \right) \right], \quad (9)$$

Since the formulation is isothermal, the specific form of the vibrational term, $\hat{\eta}_{vib}(T)$, is unimportant. The second term is the entropy density due to mixing (see Kittel and Kroemer [17] for details), k is the Boltzmann constant, C_a is the concentration of atoms, and C_s is the lattice site concentration. Assuming that C_s remains fixed in any material volume, i.e. $\delta C_s = \delta C_a + \delta C_v = 0$, the incremental entropy density corresponding to an increment in vacancy concentration, δC_v , at given stress and temperature can be expressed as

$$\delta \eta = -k \log \left(\frac{C_v}{C_a} \right) \delta C_v. \quad (10)$$

2.1.4 The Gibbs free energy density

At the given state of stress and temperature, the incremental Gibbs free energy density corresponding to increments $\delta\boldsymbol{\varepsilon}$ and δC_v is defined as

$$\delta g = \delta e - \delta w_{ext} - T\delta\eta. \quad (11)$$

With this, the constitutive relations can be obtained in a systematic fashion as outlined in the following section.

Remark 1: Since free surfaces and grain boundaries are considered, there are accompanying surface and grain boundary energies, γ_s and γ_{gb} . These energies are taken to be independent of the strain and vacancy concentration for this formulation, and therefore do not appear in the incremental Gibbs free energy density.

2.2 Constitutive relations

Anisotropic elasticity is assumed and the relation between the stress, $\boldsymbol{\sigma}$, and the elastic strain, $\boldsymbol{\varepsilon}^e$, is given by (5). The relation between the current density, \mathbf{i} , and the electric potential, ψ , is given by Ohm's law:

$$\mathbf{i} = -\frac{\nabla\psi}{\rho}, \quad (12)$$

where ρ is the electric resistivity.

2.2.1 The chemical potential of vacancies

The vacancy chemical potential is defined in the usual fashion [18]:

$$\mu_v\delta C_v = \mu_v^{eq}\delta C_v + \delta g, \quad (13)$$

where μ_v^{eq} is a constant reference potential. Applying (13) to (6–11) gives

$$\mu_v = \mu_v^{eq} + e_v^f + (\mathbb{C} : \boldsymbol{\varepsilon}^e) : \frac{1}{3}(1-f)\Omega\mathbf{1} - \frac{3}{2}(\mathbf{n} \cdot \boldsymbol{\sigma} \mathbf{n})f\Omega\chi + q\psi + kT \log\left(\frac{C_v}{C_a}\right). \quad (14)$$

The coupling with mechanics is evident through the strain- and stress-dependent terms.

2.2.2 The vacancy flux

The vacancy flux is obtained from (14) via the relation

$$\mathbf{j}_v = -\frac{D_v C_v}{kT} \nabla\mu_v, \quad (15)$$

where D_v is the vacancy diffusivity. This relation has been derived from an atomic basis by Bardeen [19]. The term $D_v C_v/kT$ is the mobility of a vacancy and $-\nabla\mu_v$, the force acting on it, is the driving force for mass transport.

2.3 Governing equations

The constitutive relations established above are incorporated in balance laws for mechanics, electric flow and mass transport, leading to a coupled system of governing differential equations.

2.3.1 Mechanics

Neglecting dynamic effects and body forces, the mechanics problem is governed by the quasistatic equilibrium equation and appropriate boundary conditions:

$$\nabla \cdot \boldsymbol{\sigma} = \mathbf{0}, \quad \text{in } \mathcal{B}, \quad (16a)$$

$$\mathbf{u} = \bar{\mathbf{u}}, \quad \text{on } \partial\mathcal{B}_{\mathbf{u}}, \quad (16b)$$

$$\boldsymbol{\sigma}\mathbf{n} = \bar{\mathbf{t}}, \quad \text{on } \partial\mathcal{B}_{\boldsymbol{\sigma}}, \quad (16c)$$

where \mathcal{B} is the domain of interest and the boundary subsets $\partial\mathcal{B}_{\mathbf{u}}$ and $\partial\mathcal{B}_{\boldsymbol{\sigma}}$ have essential and natural boundary conditions specified, respectively. These subsets satisfy $\partial\mathcal{B}_{\mathbf{u}} \cap \partial\mathcal{B}_{\boldsymbol{\sigma}} = \emptyset$ and $\overline{\partial\mathcal{B}_{\mathbf{u}} \cup \partial\mathcal{B}_{\boldsymbol{\sigma}}} = \partial\mathcal{B}$.

2.3.2 Electric flow

The electric flow problem is governed by the charge conservation equation with Dirichlet and Neumann boundary conditions:

$$\nabla \cdot \mathbf{i} = 0, \quad \text{in } \mathcal{B}, \quad (17a)$$

$$\psi = \bar{\psi}, \quad \text{on } \partial\mathcal{B}_{\psi}, \quad (17b)$$

$$\mathbf{i} \cdot \mathbf{n} = \bar{i}_i, \quad \text{on } \partial\mathcal{B}_i, \quad (17c)$$

where $\partial\mathcal{B}_{\psi} \cap \partial\mathcal{B}_i = \emptyset$ and $\overline{\partial\mathcal{B}_{\psi} \cup \partial\mathcal{B}_i} = \partial\mathcal{B}$.

2.3.3 Mass Transport

The mass-transport problem is governed by the continuity equation for vacancies, and appropriate initial and boundary conditions:

$$\frac{\partial C_v}{\partial t} = -\nabla \cdot \mathbf{j}_v - \frac{1}{\tau}(C_v - C_v^{eq})\chi, \quad \text{in } \mathcal{B}, \quad t \geq 0, \quad (18a)$$

$$C_v = C_v^0, \quad \text{in } \mathcal{B}, \quad t = 0, \quad (18b)$$

$$C_v = \bar{C}_v, \quad \text{on } \partial\mathcal{B}_{C_v}, \quad t \geq 0, \quad (18c)$$

$$\mathbf{j}_v \cdot \mathbf{n} = \bar{j}_v, \quad \text{on } \partial\mathcal{B}_{j_v}, \quad t \geq 0, \quad (18d)$$

where $\partial\mathcal{B}_{C_v}$ and $\partial\mathcal{B}_{j_v}$ are the boundary subsets on which concentration and flux boundary conditions are specified, respectively. Here, the boundary subsets satisfy $\partial\mathcal{B}_{C_v} \cap \partial\mathcal{B}_{j_v} = \emptyset$ and $\overline{\partial\mathcal{B}_{C_v} \cup \partial\mathcal{B}_{j_v}} = \partial\mathcal{B}$. The effectiveness of vacancy sources and sinks is characterized by the relaxation time, τ . The equilibrium vacancy concentration, C_v^{eq} , is defined by $\mu_v|_{C_v^{eq}} = \mu_v^{eq}$ in (14).

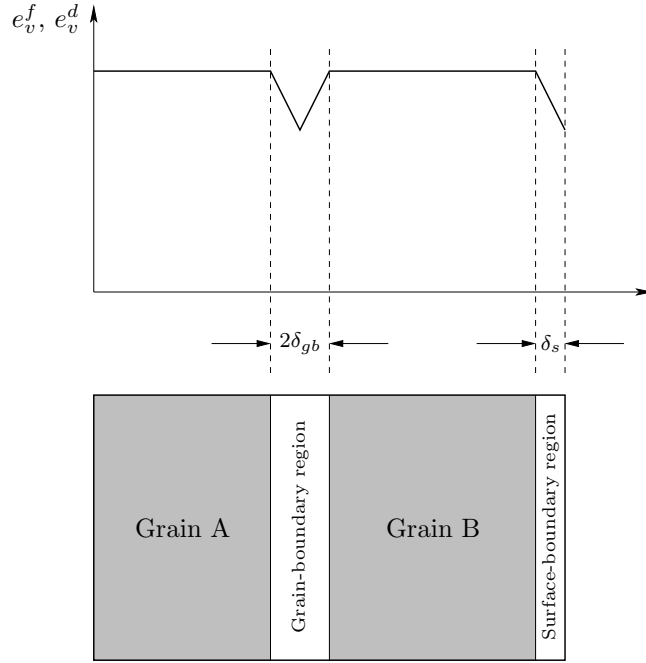


Figure 2: Variation of e_v^f and e_v^d across boundary regions.

2.4 Grain-boundary migration

The current location of a migrating grain boundary determines the value of the indicator function, $\chi(\mathbf{x}, t)$ [see Eq. (8)]; i.e. it determines whether vacancy sources/sinks are active and whether creep strain can accumulate at a given point, $\mathbf{x} \in \mathcal{B}$. Furthermore, information about the location of the boundary is needed to calculate the value of the vacancy formation energy, e_v^f , and the activation energy for diffusion, e_v^d , everywhere in the domain of interest. These properties are assumed to vary linearly over the width of a boundary region as shown in Fig. 2.

The foregoing illustrates the influence of grain-boundary migration on mass transport. Due to the tight coupling between mass transport and mechanics, the migration of the grain boundary also affects the stress. In turn, mass transfer across the grain boundary causes one grain to grow at the expense of its neighbor and thus leads to grain-boundary migration.

2.4.1 Thermodynamic driving forces

Generally, interface migration in polycrystals is driven by the accompanying decrease in the free energy of the system. The thermodynamic driving force for

such a process, acting on a unit area of the interface, is thus defined as

$$p = -\frac{\delta\mathcal{G}}{\delta V}, \quad (19)$$

where $\delta\mathcal{G}$ is the increase in the total Gibbs free energy of the system brought about by a motion of the interface, during which the interface sweeps through the volume δV . Neglecting triple junctions, the Gibbs free energy of a polycrystal can be expressed as the sum of two contributions:

$$\mathcal{G} = \int_{\mathcal{B}} g \, dV + \sum_i \int_{\Gamma_i} \gamma_i \, dS, \quad (20)$$

where g is the Gibbs free energy density as defined in (11) and γ_i is the energy per unit area of an interface, Γ_i . The term ‘‘interface’’ is used here to refer to free surfaces as well as grain boundaries, and the summation in (20) is over all such interfaces in the polycrystal.

In situations where the Gibbs free energy density, g , suffers a decrease across a grain boundary, the total free energy of the system can be reduced if the grain with the smaller value of g (evaluated at the grain boundary) were to grow at the expense of its neighbor. Thus, a driving force acts on the grain boundary. For example, during recrystallization, annealed grains grow at the expense of cold-worked grains in which large dislocation densities lead to high values of g . The misorientation between two adjacent grains of an elastically anisotropic material subjected to a directional load causes one grain to store a smaller amount of strain energy per unit volume than its neighbor. This leads to strain-induced grain-boundary migration. Electromigration also causes atoms to jump across grain boundaries and thus leads to the migration of these boundaries [20].

Under the current formulation, the driving force discussed above can be characterized as follows: When a single atom hops across the grain boundary, it exchanges positions with a vacancy. Therefore, the volume change associated with this hopping event is $\delta V = (1 - f)\Omega$. The decrease in the Gibbs free energy of the system is equal to the difference in the chemical potential of atoms across the boundary; i.e. $-\delta\mathcal{G} = \Delta\mu_a$, or equivalently $-\delta\mathcal{G} = -\Delta\mu_v$. Hence, from Eq. (19), and assuming that the chemical potential gradient across the boundary is essentially linear [21], the driving force, p_g , can be expressed as

$$p_g = \frac{-\Delta\mu_v}{(1 - f)\Omega} \approx \frac{(-\nabla\mu_v \cdot \mathbf{n})2\delta_{gb}}{(1 - f)\Omega}, \quad (21)$$

where \mathbf{n} is the unit normal to the grain boundary and $2\delta_{gb}$ is its width.

From Eq. (20), it is clear that the total Gibbs free energy of a polycrystal can also be lowered by decreasing the total surface area of the grain boundaries in the system. When a curved interface moves away from its center of curvature,

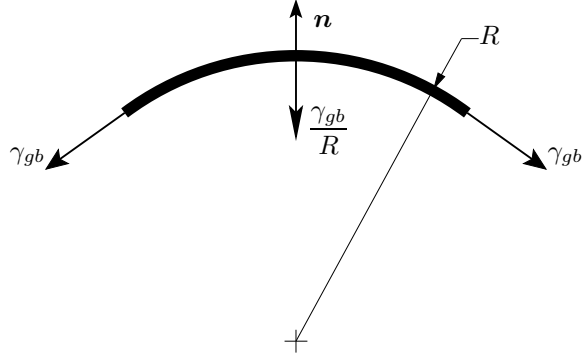


Figure 3: Driving force on a cylindrical grain boundary with a radius of curvature, R , due to surface tension, γ_{gb} .

sweeping through an increment of volume δV , the free energy of the system increases by

$$\delta\mathcal{G} = \gamma_i \left(\frac{1}{R_1} + \frac{1}{R_2} \right) \delta V, \quad (22)$$

where γ_i is the (constant) specific surface energy of the interface and R_1 and R_2 are its principal radii of curvature. This expression can be traced back to Herring [22]. It follows that, in the current two-dimensional formulation, the driving force acting on a unit area of a (cylindrical) grain boundary, due to this effect, can be expressed as

$$p_\gamma = -\frac{\gamma_{gb}}{R}, \quad (23)$$

where R is the radius of curvature and the negative sign indicates that p_γ drives the boundary to migrate *toward* its center of curvature (see Fig. 3). In a polycrystal comprising only annealed grains, the action of p_γ leads to normal grain growth; i.e. the growth of large grains at the expense of smaller ones. By contrast, in the early stages of recrystallization, small annealed grains grow at the expense of the surrounding matrix of cold-worked material. In this case, the boundaries surrounding the annealed grains move *away* from their respective centers of curvature under the effect of p_g .

2.4.2 Kinetic law

Assuming that grain-boundary migration takes place as a result of individual atoms hopping across the boundary, the migration velocity can be expressed in the following form:

$$v_n = Mp, \quad (24)$$

where v_n is in the direction of the local unit normal, \mathbf{n} , which is assumed to point away from the boundary's center of curvature and M is the grain-boundary mobility. This classical result, derived by Turnbull [21] using absolute reaction rate theory, holds provided that $p\Omega \ll kT$, a condition which is always met in grain growth and recrystallization [23]. The results of molecular dynamics simulations of curvature-driven [24] and strain-induced [25] grain-boundary migration in bicrystals agree with Eq. (24), which can be modified as follows, to account for both types of driving forces discussed in Section 2.4.1:

$$v_n = M_g p_g + M_\gamma p_\gamma. \quad (25)$$

2.4.3 Grain-boundary mobility

In Section 2.4.1, it was established that diffusion of atoms across a grain boundary due to the local gradient in the atomic chemical potential causes the boundary to migrate. The driving force for boundary migration in this case, denoted p_g , is given by (21). An expression for the corresponding mobility, M_g , can be obtained by stipulating that, in this case, the migration velocity in the direction of the local unit normal, \mathbf{n} , should be given by (see Porter and Easterling [26])

$$M_g p_g = -(\mathbf{j}_a \cdot \mathbf{n}) \Omega - (\mathbf{j}_v \cdot \mathbf{n}) f \Omega, \quad (26)$$

where \mathbf{j}_a and \mathbf{j}_v are, respectively, the local atomic and vacancy fluxes. Also recall that Ω is the atomic volume and $f\Omega$ is the volume of a vacancy. Since atoms and vacancies move by exchanging positions; i.e. $\mathbf{j}_v = -\mathbf{j}_a$, we have

$$M_g p_g = (\mathbf{j}_v \cdot \mathbf{n}) (1 - f) \Omega. \quad (27)$$

Finally, by combining (27), (21) and (15), we obtain

$$M_g = \frac{D_v C_v (1 - f)^2 \Omega^2}{2\delta_{gb} kT}. \quad (28)$$

Since grain-boundary migration under the sole influence of p_g involves *transport* across the boundary, and since, in the present treatment, mass transport is assumed to take place through the exchange of positions between atoms and vacancies, no lattice sites are transferred across the boundary in this process. By contrast, migration under the influence of p_γ consists of the transfer of lattice sites across the grain boundary [23], via the process of atoms detaching from one grain and attaching to the one on the opposite side of the boundary. It is hence unreasonable to expect the mobilities, M_g and M_γ , of these two distinctly different processes to be the same.

As mentioned earlier, normal grain growth can be attributed to the action of the driving force p_γ . The fact that grain growth is a thermally activated process suggests an Arrhenius-type relationship between the mobility, M_γ , and the temperature:

$$M_\gamma = M_0 \exp\left(\frac{-e_m}{kT}\right), \quad (29)$$

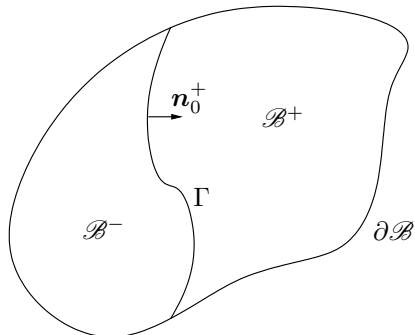


Figure 4: Schematic of the domain of the grain-boundary migration problem.

where the pre-exponential factor, M_0 , and the activation energy for grain-boundary migration, e_m , are dependent on the misorientation angle and the axis of rotation [27, 28].

Finally, by combining (23), (25), (27) and (29), we obtain the following expression for the migration velocity:

$$v_n = (\mathbf{j}_v \cdot \mathbf{n})(1 - f)\Omega - M_0 \exp\left(\frac{-e_m}{kT}\right) \frac{\gamma_{gb}}{R}. \quad (30)$$

3 Computational methods

In this section, we focus on the level-set formulation of the grain-boundary migration problem, and we present a detailed description of the computational techniques used in its implementation. The computational framework used to solve the coupled problem is based on an operator-split solution scheme and relies on the finite element method to solve the mechanics, mass-transport and electric-flow problems individually. To show how the level-set formulation is integrated into this framework, the operator-split scheme is outlined briefly in Section 3.2. A detailed description of the entire computational framework can be found elsewhere [1, 29].

3.1 Level-set formulation

Evolving interfaces can be tracked using the level set method, originally introduced by Osher and Sethian [16]. A comprehensive review of the method and the computational algorithms used in its implementation can be found in [30, 31].

Consider an evolving grain boundary, Γ , which divides the domain of interest, \mathcal{B} , into two disjoint open subsets, \mathcal{B}^- and \mathcal{B}^+ . This situation is depicted in

Fig. 4. The boundary can be parameterized with the aid of the scalar function $\phi(\mathbf{x}, t)$, defined on \mathcal{B} , provided that the following conditions are satisfied for all $t \geq 0$:

$$\phi(\mathbf{x}, t) < 0, \quad \forall \mathbf{x} \in \mathcal{B}^-, \quad (31a)$$

$$\phi(\mathbf{x}, t) = 0, \quad \forall \mathbf{x} \in \Gamma, \quad (31b)$$

$$\phi(\mathbf{x}, t) > 0, \quad \forall \mathbf{x} \in \mathcal{B}^+. \quad (31c)$$

The term *level set* refers to a set of points with a fixed value of ϕ , i.e. a contour of ϕ ; the *zero level set* represents the grain boundary. Accordingly, the unit normal to a given level set can be defined locally as

$$\mathbf{n}^+ = \frac{\nabla\phi}{\|\nabla\phi\|}, \quad (32)$$

where $\|\bullet\|$ denotes the Euclidean norm. This expression can be evaluated at any point on the zero level set to obtain the local unit normal to the boundary, \mathbf{n}_0^+ . This definition implies that \mathbf{n}_0^+ always points into the \mathcal{B}^+ region.

The evolution of the level-set field is governed by

$$\frac{\partial\phi}{\partial t} + F_n \|\nabla\phi\| = 0, \quad (33)$$

where $F_n(\mathbf{x}, t)$ is the (scalar) local propagation velocity of the level set passing through point \mathbf{x} . To track the motion of the grain boundary, we require that

$$F_n(\mathbf{x}, t) = v_n(\mathbf{x}, t), \quad \forall \mathbf{x} \in \Gamma, t \geq 0, \quad (34)$$

where v_n is obtained at any point on the grain boundary from (30). Although this requirement does not place any restrictions on the choice of F_n away from Γ , the solution procedure is simplified greatly if F_n is an *extensional* velocity field; i.e. if

$$\nabla F_n \cdot \mathbf{n}^+ = 0. \quad (35)$$

This first-order partial differential equation can be solved for F_n , at all points $\mathbf{x} \in (\mathcal{B} \setminus \Gamma)$, using (34) as a boundary condition. A simpler alternative strategy for constructing the extensional field is discussed in Section 3.1.1 below.

The level-set function, ϕ , can be initialized as the signed distance from Γ as follows:

$$\phi(\mathbf{x}, 0) = \left(\min_{\mathbf{y} \in \Gamma} \|\mathbf{x} - \mathbf{y}\| \right) \text{sign}[(\mathbf{x} - \mathbf{y}) \cdot \mathbf{n}_0^+(\mathbf{y})]. \quad (36)$$

It is noted that this initial condition satisfies (31). It also implies that initially,

$$\|\nabla\phi\| = 1, \quad \forall \mathbf{x} \in \mathcal{B}. \quad (37)$$

Importantly, this desirable mathematical property of the level-set field is preserved when the velocity field is extensional. This can be shown (see [14]) by

noting that

$$\begin{aligned}\frac{\partial}{\partial t} \|\nabla\phi\|^2 &= \frac{\partial}{\partial t} (\nabla\phi \cdot \nabla\phi) \\ &= 2\nabla\phi \cdot \frac{\partial}{\partial t} \nabla\phi.\end{aligned}\quad (38)$$

Combining (38) and (33) and assuming that ϕ and F_n are smooth, we obtain

$$\frac{\partial}{\partial t} \|\nabla\phi\|^2 = -2\nabla\phi \cdot \nabla F_n \|\nabla\phi\| - 2\nabla\phi \cdot \nabla \|\nabla\phi\| F_n. \quad (39)$$

Thus, if F_n is extensional (i.e. $\nabla\phi \cdot \nabla F_n = 0$) and ϕ is initially a signed-distance function (i.e. $\|\nabla\phi\| = 1$ and $\nabla\|\nabla\phi\| = \mathbf{0}$), we have

$$\frac{\partial}{\partial t} \|\nabla\phi\| = 0, \quad (40)$$

which implies that (37) holds for all $t \geq 0$. Hence, Eq. (33) reduces to

$$\frac{\partial\phi}{\partial t} + F_n = 0, \quad (41)$$

which governs the evolution of $\phi(\mathbf{x}, t)$ from the initial condition (36).

Recall that the mechanics, mass-transport and electric-flow problems are solved using the finite element method, and that part of the coupling between these three sub-problems, on one hand, and the grain-boundary migration sub-problem, on the other, is through the indicator function, $\chi(\mathbf{x}, t)$. In this setting, the level-set update is computed at each node via a generalized trapezoidal rule:

$$\phi(\mathbf{x}_A, t_{n+1}) = \phi(\mathbf{x}_A, t_n) - \Delta t F_n(\mathbf{x}_A, t_{n+a}), \quad (42)$$

where \mathbf{x}_A is the position vector of node A and $t_{n+a} = at_{n+1} + (1-a)t_n$, with $0 \leq a \leq 1$. It is noted that when explicit time integration is used ($a = 0$), the update operation is trivial since v_n , and hence F_n , are determined from the known solution at $t = t_n$ and do not depend on $\phi(\mathbf{x}, t_{n+1})$.

Additionally, χ is defined more precisely as follows:

$$\chi(\mathbf{x}, t) = H(\delta_{gb} - |\phi(\mathbf{x}, t)|), \quad (43)$$

where $H(\bullet)$ is the Heaviside unit step function.

3.1.1 Velocity projection and field re-initialization

The approach adopted here for constructing the extensional level-set propagation velocity field, F_n , is based on the notion that $F_n(\mathbf{x}) = v_n(\bar{\mathbf{y}})$ for any $\mathbf{x} \notin \Gamma$, if $\bar{\mathbf{y}}$ is such that

$$\|\mathbf{x} - \bar{\mathbf{y}}\| = \min_{\mathbf{y} \in \Gamma} \|\mathbf{x} - \mathbf{y}\|. \quad (44)$$

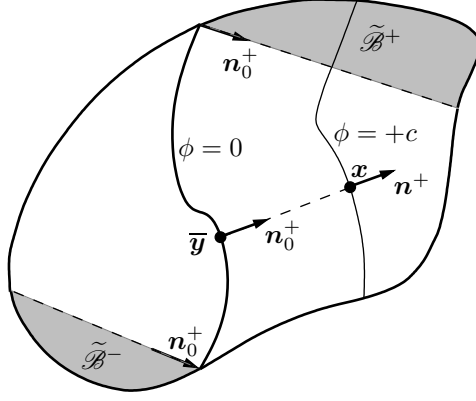


Figure 5: Construction of the extensional velocity field by velocity projection.

It is clear that the resulting velocity field satisfies (35) when

$$\mathbf{n}_0^+(\bar{\mathbf{y}}) = \frac{\mathbf{x} - \bar{\mathbf{y}}}{\|\mathbf{x} - \bar{\mathbf{y}}\|}, \quad (45)$$

as depicted in Fig. 5. This is not always the case however; for instance, if $\mathbf{x} \in \tilde{\mathcal{B}}^+$ (see Fig. 5), then $\bar{\mathbf{y}}$ is such that

$$\|\mathbf{x} - \bar{\mathbf{y}}\| = \min_{\mathbf{y} \in (\Gamma \cap \partial \mathcal{B})} \|\mathbf{x} - \mathbf{y}\|. \quad (46)$$

It follows that, for all $\mathbf{x} \in \tilde{\mathcal{B}}^+$, $F_n(\mathbf{x}) = \text{const.}$, i.e. $\nabla F_n = \mathbf{0}$, which clearly satisfies (35) also. The above arguments apply in $\tilde{\mathcal{B}}^-$ as well. This approach was first introduced by Malladi *et al.* [32] and was previously used by Garikipati and Rao [33]. A survey of alternative strategies can be found in [34].

Due to the accumulation of numerical error, the level-set field may develop perturbations; i.e. $\|\nabla \phi\|$ may deviate from unity in some regions within \mathcal{B} . The field must be re-initialized to neutralize these perturbations and retain accuracy by maintaining $\|\nabla \phi\| = 1$ [see Eqs. (38–40)]. Box 1 shows the algorithm used to implement the velocity projection scheme outlined above and the re-initialization scheme based on Eq. (36). It is obvious that the re-initialization operation consists of one trivial assignment operation per node and thus incurs almost no additional computational cost. It can therefore be performed in every time step. It must be noted that, to preserve the integrity of the solution, the re-initialization procedure must not change the current location of Γ . In other words, the re-initialized field must have the same zero level set as the original (perturbed) field. This can be achieved by leaving the value of ϕ unchanged at nodes lying within a narrow band surrounding Γ ; e.g. by setting *tolerance* = $2h$ in Box 1, where h is the mesh parameter. An elegant alternative re-initialization procedure is described in detail in [35, 36].

```

FOR each node,  $A$ , DO
  SET  $D[A] = +\infty$ 
  SET  $F[A] = 0$ 
ENDDO
FOR each segment,  $L_0$ , of the zero level set DO
  FOR each node,  $A$ , (with position vector  $\mathbf{x}_A$ ) DO
    FIND point  $\bar{\mathbf{z}} \in L_0$  such that
       $\|\mathbf{x}_A - \bar{\mathbf{z}}\| = \min_{\mathbf{z} \in L_0} \|\mathbf{x}_A - \mathbf{z}\|$ 
    IF  $\|\mathbf{x}_A - \bar{\mathbf{z}}\| < |D[A]|$  THEN
      COMPUTE  $v_n(\bar{\mathbf{z}})$  using Eq. (30)
      COMPUTE  $\mathbf{n}_0^+(\bar{\mathbf{z}})$  using Eq. (32)
      SET  $F[A] = v_n(\bar{\mathbf{z}})$ 
      SET  $D[A] = \|\mathbf{x}_A - \bar{\mathbf{z}}\| \text{sign}[(\mathbf{x}_A - \bar{\mathbf{z}}) \cdot \mathbf{n}_0^+(\bar{\mathbf{z}})]$ 
    ENDIF
  ENDDO
ENDDO
FOR each node,  $A$ , DO
  IF  $\Phi[A] > \textit{tolerance}$  AND  $\mathbf{x}_A \notin (\tilde{\mathcal{B}}^+ \cup \tilde{\mathcal{B}}^-)$  THEN
    RE-INITIALIZE  $\Phi[A] = D[A]$ 
  ENDIF
ENDDO

```

Box 1: Velocity projection and level-set field re-initialization algorithm. Here, the global arrays, Φ , F and D hold the nodal values of ϕ , F_n and $\|\mathbf{x} - \mathbf{y}\|$, respectively. A division of the zero level set which spans a single element is referred to as a “segment” and is denoted by L_0 . Also, since bilinear shape functions are used, an element can contain only one such segment.

3.1.2 Gradient smoothing

The local migration velocity, v_n , on the grain boundary is dependent on the local curvature, $\kappa = 1/R$, which is defined as follows:

$$\kappa = \nabla \cdot \mathbf{n}^+. \quad (47)$$

From (32) and (37), it is clear that $\mathbf{n}^+ = \nabla\phi$, and the curvature can hence be expressed as

$$\kappa = \nabla^2\phi = \sum_{i=1}^{n_{sd}} \frac{\partial^2\phi}{\partial x_i \partial x_i}, \quad (48)$$

where $n_{sd} = 2$ is the number of spatial dimensions. Since the value of ϕ is updated at the finite element nodes, it is convenient to use the shape functions to evaluate the spatial derivatives in the above expression. However, since bilinear shape functions are used for simplicity and robustness, the obtained curvature

is identically zero everywhere in the domain. To overcome this difficulty, we introduce a ‘smoothed’ normal vector field $\tilde{\mathbf{n}}^+$, weakly related to $\nabla\phi$ by

$$\int_{\mathcal{B}} \mathbf{w} \cdot (\tilde{\mathbf{n}}^+ - \nabla\phi) \, dV = 0, \quad (49)$$

where \mathbf{w} is an arbitrary weighting function. Equivalently, the nodal values of each component, \tilde{n}_i^+ , of the smoothed normal vector can be obtained by minimizing the following discretized functional:

$$\sum_{e=1}^{n_{el}} \int_{\mathcal{B}^e} \left[\sum_{A=1}^{n_{en}} \left(N_A \tilde{n}_i^+(\mathbf{x}_A) - \frac{dN_A}{dx_i} \phi(\mathbf{x}_A) \right) \right]^2 \, dV, \quad (50)$$

where n_{el} is the number of elements in the model, \mathcal{B}^e denotes an element domain, n_{en} is the number of nodes per element and N_A is the shape function associated with node A . This leads to a matrix equation of the form $\mathbf{M}\mathbf{d} = \mathbf{f}$, where \mathbf{d} is the global vector containing the nodal values of the component \tilde{n}_i^+ . The global mass matrix, \mathbf{M} , and right-hand side vector, \mathbf{f} , are obtained from the corresponding element arrays via the usual assembly process. The element arrays in this case are given by

$$m_{AB}^e = \int_{\mathcal{B}^e} N_A N_B \, dV, \quad (51a)$$

$$f_A^e = \int_{\mathcal{B}^e} N_A \sum_{B=1}^{n_{en}} \frac{dN_B}{dx_i} \phi(\mathbf{x}_B) \, dV. \quad (51b)$$

Finally, the curvature is evaluated as follows:

$$\kappa = \sum_{A=1}^{n_{en}} \sum_{i=1}^{n_{sd}} \frac{dN_A}{dx_i} \tilde{n}_i^+(\mathbf{x}_A). \quad (52)$$

Remark 2: This approach is formally equivalent to a two-field mixed formulation for ϕ and $\tilde{\mathbf{n}}^+$ (see Zienkiewicz and Taylor [37]).

3.2 Operator-split algorithm

The coupled problem is solved using an operator-split algorithm. The sequence of operations carried out in one time step is shown in Box 2 to illustrate how the level-set formulation is incorporated into this solution scheme. Details regarding the advantages, applications and numerical stability characteristics of operator-split schemes can be found in [38, 39, 40] and references therein.

- | |
|--|
| <p>(1) CONSTRUCT the smooth level-set gradient field, $\tilde{\mathbf{n}}^+$.</p> <p>(2) CONSTRUCT the extensional velocity field, F_n, and RE-INITIALIZE the level-set field (see Box 1).</p> <p>(3) PERFORM the level-set update using Eq. (42).</p> <p>(4) SOLVE the electric-flow problem for the electric potential, ψ.</p> <p>(5) REPEAT the following sequence:</p> <p style="padding-left: 2em;">(a) SOLVE the mechanics problem for the displacements, \mathbf{u}.</p> <p style="padding-left: 2em;">(b) SOLVE the mass transport (composition) problem for the vacancy concentration, C_v.</p> <p style="padding-left: 2em;">UNTIL both the mechanics and mass transport problems have converged.</p> <p>(6) INCREMENT time and GOTO step (1).</p> |
|--|

Box 2: The operator-split algorithm used to solve the coupled problem.

4 Numerical examples

Numerical results, obtained by solving the coupled initial and boundary value problem, are presented here with the aim of highlighting some of the advantages of the current approach. A $1\ \mu\text{m}$ wide, $2.5\ \mu\text{m}$ long segment of an aluminum interconnect line is modeled. The values of the material parameters used for Al are given in Table 1. The segment consists of two pure Al crystals separated by a $\Sigma 7$ tilt grain boundary (38.2° misorientation about $\langle 111 \rangle$).

The line is assumed to operate at $T = 373\ \text{K}$, with a reference temperature, $T_0 = 473\ \text{K}$. Rigid passivation material surrounding the line prevents vacancies from crossing the upper and lower boundaries of the domain (see Fig. 6a); i.e. the condition $\mathbf{j}_v \cdot \mathbf{n} = 0$ holds at these boundaries. Periodic boundary conditions are imposed on the vacancy concentration at the left and right boundaries of the segment and an electrostatic potential difference, $\Delta\psi = 0.0021\ \text{V}$, is applied between these two extremities. Vacancies drift along the electric field, $\mathbf{E} = -\nabla\psi$, pointing to the right.

In the first example, the migrating grain boundary consists, initially, of two straight (planar) sections, which are joined by a circular (cylindrical) section. The straight sections form 45° angles with the upper and lower boundaries of the domain as shown in Fig. 6a. Since the vacancy formation energy, e_v^f , is low inside grain-boundary regions where vacancy sources are also present, vacancies accumulate in such regions resulting in high values of the local vacancy concentration, C_v . The location of the grain boundary is revealed locally by the maximum-valued contour of C_v .

Figure 6 shows the evolution of the vacancy concentration contours in the line. It is clear that, during the first 300 seconds, the central cylindrical section of

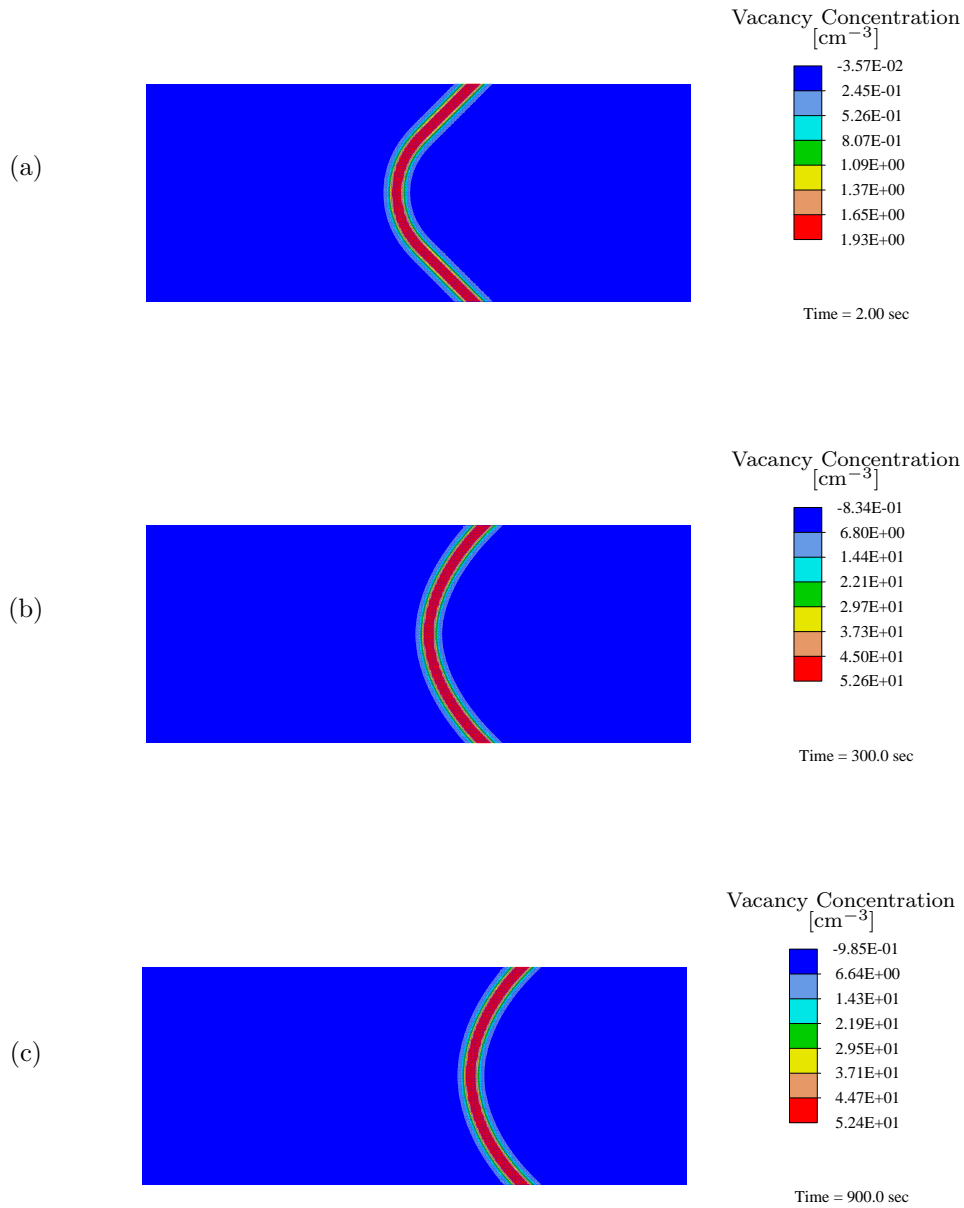


Figure 6: The evolution of the vacancy concentration contours in the interconnect line due to the motion of the grain boundary (first example). (a) $t = 2.0$ sec. (b) $t = 300.0$ sec. (c) $t = 900.0$ sec.

Table 1: Material properties of Al (thin film) used in the analysis

Parameter		Value	Unit
Elastic moduli	c_{11}	184.7	GPa
	c_{12}	95.15	GPa
	c_{44}	44.7	GPa
Linear coefficient of thermal expansion	α	24×10^{-6}	K^{-1}
Electric resistivity	ρ	4.2×10^{-8}	$\Omega\cdot\text{m}$
Apparent electric charge on a vacancy	q	5.6077×10^{-19}	C
Atomic volume in the absence of strain	Ω_0	16.61	\AA^3
Vacancy-atom volume ratio	f	0.8	
Vacancy formation energy in the bulk	e_v^f	0.67	eV
Minimum value of e_v^f in boundary regions*		0.5433	eV
Activation energy for diffusion in the bulk	e_v^d	1.47	eV
Minimum value of e_v^d in boundary regions*		1.1090	eV
Grain-boundary width	$2\delta_{gb}$	0.198	μm
Diffusivity premultiplier [†]	D_{v_0}	2.6×10^3	$\text{m}^2\cdot\text{s}^{-1}$
Reduced grain-boundary mobility premultiplier [‡]	A_0	39.81	$\text{m}^2\cdot\text{s}^{-1}$
Activation energy for grain-boundary migration	e_m	1.29	eV

* See Fig. 2.
[†] The diffusivity is given by $D_v = D_{v_0} \exp(-e_v^d/kT)$.
[‡] $A_0 = \gamma_{gb}M_0$; also see Eqs. (29) and (30).

the boundary migrates to the right; i.e. toward its center of curvature, while the planar sections are relatively less mobile (Fig. 6b). It must be emphasized that the interaction between mechanics, mass transport, electric effects and grain-boundary motion is accounted for, and the driving force for boundary migration, due to stress-driven diffusion and electromigration, is included in the calculations. However, its effect is overshadowed by the dominant driving force due to the curvature of the boundary.

After 900 seconds, the curvature is approximately the same everywhere on the grain boundary (Fig. 6c). At this stage, a steady state prevails and the boundary continues to travel toward the right without undergoing any further changes in shape. It is noted that the level set calculations remain stable. The boundary remains smooth and does not develop any spurious cusps or ripples. The 45° equilibrium angles between the grain boundary and the sidewalls are maintained as the solution progresses.

A vector plot of the vacancy flux field at $t = 300$ sec and a corresponding contour plot of the magnitude of the vacancy flux are shown in Figs. 7 and 8, respectively. It is clear that a strong vacancy flux exists in the neighborhood of the boundary and, although the field is complicated in this neighborhood, it can be seen that vacancies tend to drift in the same direction as the migrating

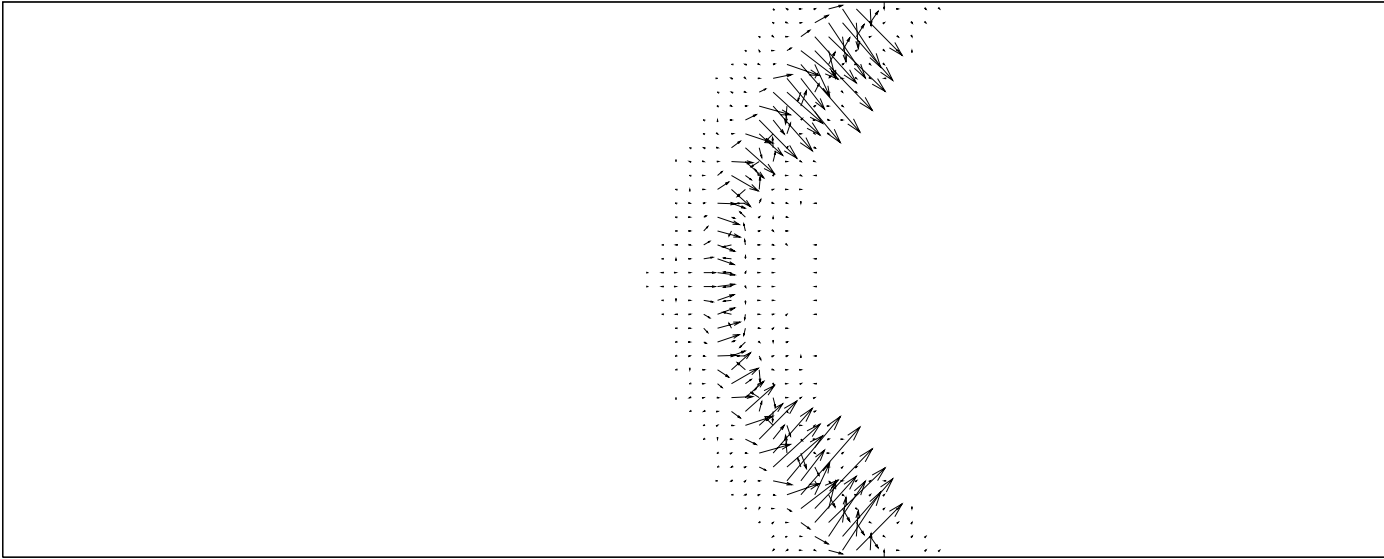


Figure 7: Vector plot of the vacancy flux, \mathbf{j}_v , in the line at $t = 300$ sec (first example). Also see Fig. 8 for magnitude of \mathbf{j}_v .

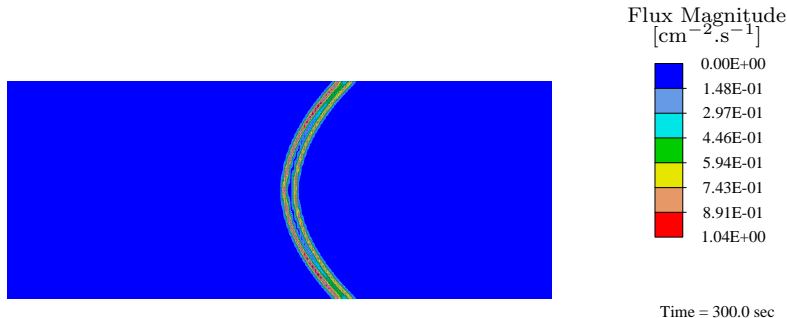


Figure 8: Contours of the magnitude of the vacancy flux, $\|\mathbf{j}_v\|$, in the line (first example).

boundary, thus preventing the appearance of a “trail” of vacancies or other oscillations in the numerical solution in the boundary’s wake. It is important to note that the flux field evolves continually as the boundary migrates. It is also notable that the formulation captured this aspect of the coupling between mass transport and grain-boundary migration without additional terms being added to the expression of the vacancy flux to account, specifically, for the effect of moving boundaries.

The second example is concerned with the case where a curved grain boundary evolves into a planar configuration to reduce the free energy of the system. Here, the equilibrium angles at the grain boundary-sidewall intersections are set to 90° and the initial geometry of the boundary is different and less regular than in the first example. It is clear from Fig. 9, which shows the evolution of the vacancy concentration contours in this case, that the boundary flattens as the solution progresses. It is noted that the equilibrium angles are also preserved in this case. It is also noted that in this case, perturbations in the solution lead to the formation of spurious “shadow” regions ($\tilde{\mathcal{B}}^+$, $\tilde{\mathcal{B}}^-$; see Fig. 5) and re-initialization becomes necessary in these regions to maintain accuracy and to preserve the contact angles.

Although the numerical stability characteristics of the level-set formulation—and those of the operator-split algorithm—are not examined in a formal setting, no spatial or temporal oscillations are observed in the numerical solution of the example problems presented, as long as the time-step size is within the CFL limit; i.e. $\Delta t < h/F_n$, where h is the mesh parameter. Moreover, numerical experiments suggest that oscillation-free results can be obtained in some cases where the migrating interface develops sharp corners, without adding a shock-capturing operator such as the one described in [41, 42, 43]. Such stability-related issues will be examined in a forthcoming paper.

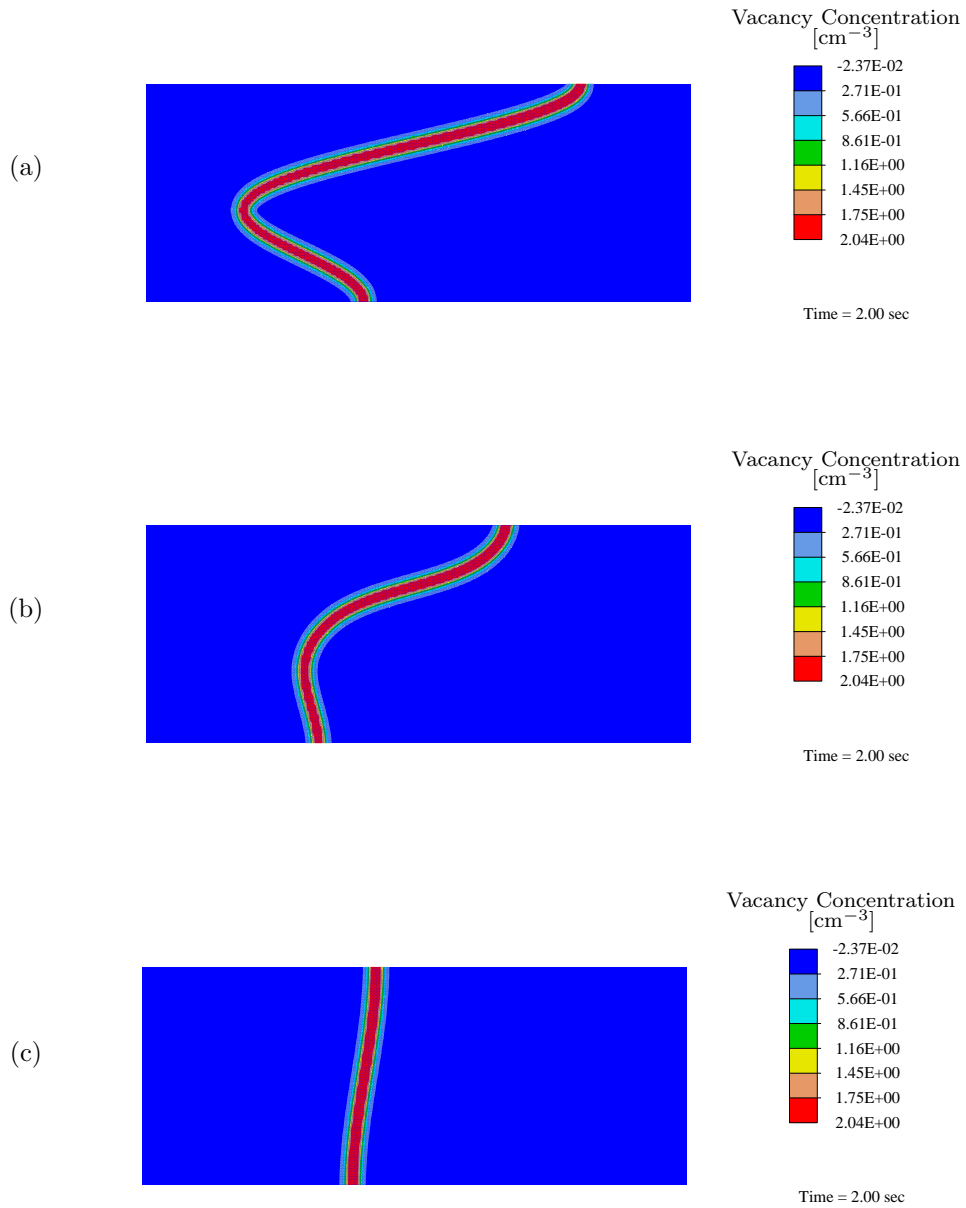


Figure 9: The evolution of the vacancy concentration contours in the interconnect line due to the motion of the grain boundary (second example). (a) $t = 2.0$ sec. (b) $t = 200.0$ sec. (c) $t = 1500.0$ sec.

5 Summary

The coupled continuum formulation presented here was developed to model stress-driven self-diffusion and electromigration in polycrystals while accounting fully for the interaction between these mass transfer processes and the motion of grain boundaries. The formulation accounts for two distinct thermodynamic driving forces acting on a grain boundary; one due to the boundary’s own curvature and another engendered by mass transfer across the boundary via stress-driven self-diffusion and electromigration.

The level set method is used to pose grain-boundary migration as a time-dependent field problem governed by a pure advection equation. Instead of resorting to widely used spatial stabilization techniques (e.g. upwinding schemes, Galerkin/Least-Squares) to attenuate the spurious oscillations known to appear in the numerical solution of equations of this type, the level-set equation is reduced to an ordinary differential equation using the mathematical properties of signed distance functions and extensional velocity fields. The use of an explicit time-integration scheme also eliminates the need for an iterative solution method. Thus, advancing the solution in time is achieved by updating the value of the level-set function at each nodal point separately. The algorithm used to construct the extensional velocity field—and to re-initialize the level-set field simultaneously for increased efficiency—is also presented. Furthermore, a least-squares projection technique is used to allow the local curvature of the grain boundary to be calculated directly from the level-set field without resorting to higher-order interpolation. A detailed description of this least-squares smoothing technique, which is analogous to stress-recovery methods, is provided.

The numerical examples presented indicate that the strong coupling in the problem is captured adequately and that the numerical implementation allows the solution of the coupled initial- and boundary-value problem to be advanced in time in a stable fashion to obtain physically meaningful results.

Acknowledgments

We would like to acknowledge useful discussions with Prof. G. M. Hulbert of the University of Michigan.

This work was supported by the National Science Foundation under grant #CMS0075989.

References

- [1] K. Garikipati, L. C. Bassman, and M. D. Deal, “A lattice-Based Micromechanical Continuum Formulation for Stress-Driven Mass Transport in Poly-

- crystalline Solids,” *J. Mech. Phys. Solids*, vol. 49, no. 6, pp. 1209–1237, 2001.
- [2] K. Garikipati and L. C. Bassman, “Atomically-Based Field Formulations for Coupled Problems of Composition and Mechanics,” in *MRS Symposium Proceedings, Multiscale Modeling of Materials–2000* (L. P. Kubin, J. L. Bassani, K. Cho, H. Gao, and R. L. B. Selinger, eds.), vol. 653, (Warrendale), pp. Z9.6.1–Z9.6.6, Materials Research Society, 2001.
- [3] F. Larché and J. W. Cahn, “A Linear Theory of Thermochemical Equilibrium of Solids Under Stress,” *Acta Metall.*, vol. 21, no. 8, pp. 1051–1063, 1973.
- [4] F. C. Larché and J. W. Cahn, “The Interactions of Composition and Stress in Crystalline Solids,” *Acta Metall.*, vol. 33, no. 3, pp. 331–357, 1985.
- [5] W. D. Nix, “Effects of Grain Shape on Nabarro-Herring and Coble Creep Processes,” *Met. Forum*, vol. 4, no. 1–2, pp. 38–43, 1981.
- [6] J. P. Hirth and W. D. Nix, “Analysis of Cavity Nucleation in Solids Subjected to External and Internal Stresses,” *Acta Metall.*, vol. 33, no. 3, pp. 359–368, 1985.
- [7] F. Y. Génin, “The Initial Stages of the Formation of Holes and Hillocks in Thin Films Under Equal Biaxial Stress,” *Acta Metall. Mater.*, vol. 43, no. 12, pp. 4289–4300, 1995.
- [8] A. F. Bower and L. B. Freund, “Finite Element Analysis of Electromigration and Stress Induced Diffusion in Deformable Solids,” in *MRS Symposium Proceedings, Materials Reliability in Microelectronics V* (A. S. Oates, K. Gadepally, R. Rosenberg, W. F. Filter, and A. L. Greer, eds.), vol. 391, (Pittsburgh), pp. 177–188, Materials Research Society, 1995.
- [9] L. Xia, A. F. Bower, Z. Suo, and C. F. Shih, “A Finite Element Analysis of the Motion and Evolution of Voids Due to Strain and Electromigration Induced Surface Diffusion,” *J. Mech. Phys. Solids*, vol. 45, no. 9, pp. 1473–1493, 1997.
- [10] B. Sun and Z. Suo, “Finite Element Method for Simulating Interface Motion – I. Migration of Phase and Grain Boundaries,” *Acta Mater.*, vol. 45, no. 5, pp. 1907–1915, 1997.
- [11] B. Sun and Z. Suo, “Finite Element Method for Simulating Interface Motion – II. Large Shape Change Due to Surface Diffusion,” *Acta Mater.*, vol. 45, no. 12, pp. 4953–4962, 1997.
- [12] A. C. F. Cocks and S. P. A. Gill, “A Variational Approach to Two Dimensional Grain Growth – I. Theory,” *Acta Mater.*, vol. 44, no. 12, pp. 4765–4775, 1996.

- [13] S. P. A. Gill and A. C. F. Cocks, “A Variational Approach to Two Dimensional Grain Growth – II. Numerical Results,” *Acta Mater.*, vol. 44, no. 12, pp. 4777–4789, 1996.
- [14] H.-K. Zhao, T. Chan, B. Merriman, and S. Osher, “A Variational Level Set Approach to Multiphase Motion,” *J. Comput. Phys.*, vol. 127, no. 1, pp. 179–195, 1996.
- [15] F. Reitich and H. M. Soner, “Three-Phase Boundary Motions Under Constant Velocities. I. The Vanishing Surface Tension Limit,” *Proc. R. Soc. Edinb. A, Math.*, vol. 126, pp. 837–865, 1996.
- [16] S. Osher and J. A. Sethian, “Fronts Propagating with Curvature-Dependent Speed: Algorithms Based on Hamilton-Jacobi Formulations,” *J. Comput. Phys.*, vol. 79, no. 1, pp. 12–49, 1988.
- [17] C. Kittel and H. Kroemer, *Thermal Physics*. San Francisco: W. H. Freeman, second ed., 1980.
- [18] J. W. Gibbs, *The Collected Works of J. Willard Gibbs*. New York: Longmans, Green and Co., 1928.
- [19] J. Bardeen, “Diffusion in Binary Alloys,” *Phys. Rev.*, vol. 76, no. 9, pp. 1403–1405, 1949.
- [20] A. Katsman, L. Klinger, and L. Levin, “Driving Force for Grain Boundary Migration During Electromigration: Effect of Elastic Anisotropy,” *Scripta Mater.*, vol. 36, no. 4, pp. 489–493, 1997.
- [21] D. Turnbull, “Theory of Grain Boundary Migration Rates,” *Trans. Am. Inst. Min. Engrs.*, vol. 191, pp. 661–665, 1951.
- [22] C. Herring, “Surface Tension as a Motivation for Sintering,” in *The Physics of Powder Metallurgy* (W. E. Kingston, ed.), pp. 143–179, New York: McGraw-Hill, 1951.
- [23] G. Gottstein, D. A. Molodov, and L. S. Shvindlerman, “Grain Boundary Migration in Metals: Recent Developments,” *Interface Sci.*, vol. 6, no. 1–2, pp. 7–22, 1998.
- [24] M. Upmanyu, R. W. Smith, and D. J. Srolovitz, “Atomistic Simulation of Curvature Driven Grain Boundary Migration,” *Interface Sci.*, vol. 6, no. 1–2, pp. 41–58, 1998.
- [25] B. Schönfelder, D. Wolf, S. R. Phillpot, and M. Furtkamp, “Molecular-Dynamics Method for the Simulation of Grain-Boundary Migration,” *Interface Sci.*, vol. 5, no. 4, pp. 245–262, 1997.
- [26] D. A. Porter and K. E. Easterling, *Phase Transformations in Metals and Alloys*, ch. 3. Cheltenham: Nelson Thornes, second ed., 2001.

- [27] K. T. Aust and J. W. Rutter, “Temperature Dependence of Grain Boundary Migration in High-Purity Lead Containing Small Additions of Tin,” *Trans. Am. Inst. Min. Engrs.*, vol. 215, pp. 820–831, 1959.
- [28] M. Upmanyu, D. J. Srolovitz, L. S. Shvindlerman, and G. Gottstein, “Misorientation Dependence of Intrinsic Grain Boundary Mobility: Simulation and Experiment,” *Acta Mater.*, vol. 47, no. 14, pp. 3901–3914, 1999.
- [29] H. M. Mourad, *A Continuum Approach to the Modeling of Microstructural Evolution in Polycrystalline Solids*. Ph.D. dissertation, University of Michigan, 2004.
- [30] J. A. Sethian, *Level Set Methods and Fast Marching Methods*. New York: Cambridge University Press, second ed., 1999.
- [31] J. A. Sethian, “Evolution, Implementation, and Application of Level Set and Fast Marching Methods for Advancing Fronts,” *J. Comput. Phys.*, vol. 169, no. 2, pp. 503–555, 2001.
- [32] R. Malladi, J. A. Sethian, and B. C. Vemuri, “Shape Modeling with Front Propagation: A Level Set Approach,” *IEEE Trans. Pattern Anal. Mach. Intell.*, vol. 17, no. 2, pp. 158–175, 1995.
- [33] K. Garikipati and V. Rao, “Recent Advances in Models for Thermal Oxidation of Silicon,” *J. Comput. Phys.*, vol. 174, no. 1, pp. 138–170, 2001.
- [34] D. Adalsteinsson and J. A. Sethian, “The Fast Construction of Extension Velocities in Level Set Methods,” *J. Comput. Phys.*, vol. 148, no. 1, pp. 2–22, 1999.
- [35] M. Sussman, P. Smereka, and S. Osher, “A Level Set Approach for Computing Solutions to Incompressible Two-Phase Flow,” *J. Comput. Phys.*, vol. 114, no. 1, pp. 146–159, 1994.
- [36] M. Sussman and E. Fatemi, “An Efficient, Interface-Preserving Level Set Redistancing Algorithm and its Application to Interfacial Incompressible Flow,” *SIAM J. Sci. Comput.*, vol. 20, no. 4, pp. 1165–1191, 1999.
- [37] O. C. Zienkiewicz and R. L. Taylor, *The Finite Element Method*, vol. 1, ch. 11. Oxford: Butterworth-Heinemann, fifth ed., 2000.
- [38] F. Armero and J. C. Simo, “A New Unconditionally Stable Fractional Step Method for Nonlinear Coupled Thermomechanical Problems,” *Int. J. Numer. Methods Eng.*, vol. 35, no. 4, pp. 737–766, 1992.
- [39] F. Armero and J. C. Simo, “A Priori Stability Estimates and Unconditionally Stable Product Formula Algorithms for Nonlinear Coupled Thermo-plasticity,” *Int. J. Plast.*, vol. 9, no. 6, pp. 749–782, 1993.

- [40] C. A. Felippa, K. C. Park, and C. Farhat, “Partitioned Analysis of Coupled Mechanical Systems,” *Comput. Methods Appl. Mech. Eng.*, vol. 190, no. 24–25, pp. 3247–3270, 2001.
- [41] P. Hansbo, “Explicit Streamline Diffusion Finite Element Methods for the Compressible Euler Equations in Conservation Variables,” *J. Comput. Phys.*, vol. 109, no. 2, pp. 274–288, 1993.
- [42] T. J. Barth and J. A. Sethian, “Numerical Schemes for the Hamilton-Jacobi and Level Set Equations on Triangulated Domains,” *J. Comput. Phys.*, vol. 145, no. 1, pp. 1–40, 1998.
- [43] J. Chessa, P. Smolinski, and T. Belytschko, “The extended finite element method (XFEM) for solidification problems,” *Int. J. Numer. Methods Eng.*, vol. 53, no. 8, pp. 1959–1977, 2002.